PNAS RESEARCH ARTICLE | CHEMISTRY
BIOPHYSICS AND COMPUTATIONAL BIOLOGY OPEN ACCESS

# HIV-1 capsid shape, orientation, and entropic elasticity regulate translocation into the nuclear pore complex

Arpa Hudait[a] and Gregory A. Voth[a,1]

Edited by Monica Olvera de la Cruz, Northwestern University, Evanston, IL; received August 10, 2023; accepted December 6, 2023

**Nuclear import and uncoating of the viral capsid are critical steps in the HIV-1 life cycle that serve to transport and release genomic material into the nucleus. Viral core import involves translocating the HIV-1 capsid at the nuclear pore complex (NPC). Notably, the central channel of the NPC appears to often accommodate and allow passage of intact HIV-1 capsid, though mechanistic details of the process remain to be fully understood. Here, we investigate the molecular interactions that operate in concert between the HIV-1 capsid and the NPC that regulate capsid translocation through the central channel. To this end, we develop a "bottom-up" coarse-grained (CG) model of the human NPC from recently released cryo-electron tomography structure and then construct composite membrane-embedded CG NPC models. We find that successful translocation from the cytoplasmic side to the NPC central channel is contingent on the compatibility of the capsid morphology and channel dimension and the proper orientation of the capsid approach to the channel from the cytoplasmic side. The translocation dynamics is driven by maximizing the contacts between phenylalanine-glycine nucleoporins at the central channel and the capsid. For the docked intact capsids, structural analysis reveals correlated striated patterns of lattice disorder likely related to the intrinsic capsid elasticity. Uncondensed genomic material inside the docked capsid augments the overall lattice disorder of the capsid. Our results suggest that the intrinsic "elasticity" can also aid the capsid to adapt to the stress and remain structurally intact during translocation.**

HIV-1 capsid | nuclear pore complex | nucleocytoplasmic transport | antiviral drugs | coarse-grained molecular dynamics

## Significance

Nuclear pore complexes form a gate that mediates the transport of cargo between the cytoplasm and nucleus. Here, we investigate the factors regulating the nuclear entry of intact HIV-1 capsid using coarse-grained simulations and structural analysis. The central channel dynamically expands to allow capsid passage, demonstrating the pleomorphic nature of the channel necessary for transporting large cargoes. Stress induced by the central channel confinement and uncondensed internal genomic material generates correlated striated patterns of lattice disorder across the capsid surface, which are a measure of its "elasticity." Our study demonstrates that modulating the capsid lattice elasticity can be an effective strategy for the development of antiviral drugs to prevent viral nuclear import and impair infection.

HIV-1 spreads infection through a replication cycle that comprises several distinct steps. The transport of the viral genome into the nucleus is an imperative step in the life cycle for infection (1). The HIV-1 mature capsid encloses and protects the genomic RNA and the critical enzymes for replication, reverse transcriptase, and integrase (2, 3). The capsid comprises 1,000 to 1,500 copies of the capsid (CA) proteins forming a predominantly hexameric lattice while incorporating 12 pentamers (4–7). The typical capsid cone is of length ~120 nm and width ~60 nm (8, 9). Nuclear import of capsid is mediated through the NPC embedded in the nuclear envelope. Early structural studies determined the diameter of the NPC central channel that mediates cargo transport to be ~40 nm (10). Due to the incompatibility in size between the capsid cone and central channel, initial models of viral nuclear import and uncoating proposed that uncoating of the capsid is initiated in the cytoplasm or when the capsid is docked at the NPC (11–15). In contrast to the early models, recent experiments tracking the HIV-1 cores in live infected cells demonstrated that intact capsids are transported through the nuclear pore, reverse transcription occurs in the (at least largely) intact capsid, and uncoating occurs before integration in the vicinity of the genomic integration site (16, 17). This observation is also supported by direct visualization of capsids through cryo-ET (cryo-electron tomography) and electron microscopy techniques that revealed the transport of intact capsids across the nuclear pore (18, 19). At present, however, it is not known what fraction of the total capsids present in an infected cell can translocate into and through the nuclear pore, nor what structural and other characteristics the successful ones may have. Moreover, these recent findings also suggest that NPC can exist in a dilated state allowing translocation of intact capsids. How the physical properties of capsid lattice are impacted during passage into the NPC central channel is also yet to be fully understood and can provide valuable insight into the molecular mechanism of capsid structural failure and rupture after entry to the nucleus. Moreover, the nuclear import step of capsid can also be a target for ultrapotent inhibitor drugs allowing premature rupturing of the capsid prior to nuclear entry, preventing the release of the genomic material in the nucleus and therefore reducing infectivity (20, 21).

The NPC, with a molecular weight of ~120 MDa and consisting of up to 1,000 proteins, is one of the largest protein assemblies in the cell. Several recent studies have determined

Author affiliations: [a]Department of Chemistry, Chicago Center for Theoretical Chemistry, Institute for Biophysical Dynamics, and James Franck Institute, The University of Chicago, Chicago, IL 60637

Author contributions: A.H. and G.A.V. designed research; A.H. performed research; A.H. contributed new reagents/analytic tools; A.H. analyzed data; G.A.V. secured funding for research and computational resources; and A.H. and G.A.V. wrote the paper.

The authors declare no competing interest.

This article is a PNAS Direct Submission.



[1]To whom correspondence may be addressed. Email: gavoth@uchicago.edu.

This article contains supporting information online at https://www.pnas.org/lookup/suppl/doi:10.1073/pnas.2313737121/-/DCSupplemental.

Published January 19, 2024.

the structure of human NPC in unprecedented detail, allowing for a detailed view of previously unassigned segments of the complex (22–24). The constituent proteins of the NPC are called nucleoporins (NUPs). NUPs assemble to form hetero-oligomeric complexes establishing three stacked concentric rings in an eightfold rotational symmetry; each ring consists of eight spokes. The building block of the outer cytoplasmic ring (CR) and nuclear ring (NR) is the Y-complex oligomerized in a head-to-tail arrangement forming two concentric and slightly shifted eight-membered rings (10). Similarly, multiple copies of NUPs comprise a single spoke of the inner ring (IR) complex. Importantly, linker NUPs interconnect adjacent spokes of the IR complex allowing flexibility in the relative arrangement of spokes. Intrinsically disordered FG-NUPs (phenylalanine-glycine nucleoporins) tethered to the NPC scaffold are key for the nucleocytoplasmic exchange of cargo. The HIV-1 capsid is known to interact with several FG-NUPs at the CR, IR, and NR (25–27).

Simulations of membrane-embedded NPC with capsid at atomistic detail would require over a billion atoms and are presently and in the foreseeable future computationally infeasible due to the spatial and temporal scale of the multistep translocation process. Using systematically derived "bottom-up" CG (coarse-grained) models, one can instead perform physically reliable molecular dynamics (MD) simulations of large protein complexes at scales of relevance to typical cellular processes. Here, bottom-up signifies that the CG molecular model and interactions are systematically constructed from underlying atomistic interactions (28). In other words, the derived CG model and interactions are designed to reproduce the molecular behavior sampled in the atomistic simulations when the latter is projected exactly onto a coarser representation. As a leading example, CG MD simulations have been particularly effective in uncovering essential mechanistic details of large-scale viral processes, such as factors that regulate HIV-1 capsid lattice growth (7, 29, 30), capsid restriction (31), and immature Gag assembly (32, 33), and entry of severe acute respiratory syndrome coronavirus 2 (SARS-CoV-2) (34). Hence in this work, we first derive a bottom-up CG molecular model and interactions of NUP monomer and subcomplexes from the recent high-resolution structure (PDB: 7R5K and 7R5J) of human NPC (22). Additionally, we develop a CG molecular model of HIV-1 CA monomer (the same resolution as NPC) and the CG associative interactions between CA-CA and CA-FG. The CG model of NUP monomers and subcomplexes are combined to generate a composite model of constricted and dilated membrane-embedded human NPC. The composite CG NPC model developed in this work consists of the outer CR and NR, IR, and the NUPs containing the capsid-binding FG-repeats at the IR (NUP54, NUP58, and NUP62). We created another composite NPC model in which the disordered NUP98 chains are also tethered to the IR. The CG models in this work are the so-called "solvent-free" CG models in which the effects of the solvent are folded into the CG interactions. Similar models are sometimes referred to as "implicit solvent" models, but that phrase can carry a specific connotation as to how the effects of solvent are included, and often such models are expressed at full atomic resolution.

In this work, we elucidate the HIV-1 capsid translocation dynamics into the NPC central channel using CG MD simulations. Specifically, we simulate the translocation dynamics of three different capsid morphologies into the central channel of constricted and dilated states of NPC using the composite CG NPC and HIV-1 capsid CG models. Our simulations show that the dilated state of NPC allows translocation of the cone-shaped capsid into the NPC central channel when docked at the narrow end. The dilated state of NPC also allows the translocation of a pill-shaped capsid. The constricted NPC impedes the translocation of all capsid morphologies examined in the simulations. We find that capsid translocation is driven by the energetics of the interaction between the capsid-binding central channel FG-NUPs. In contrast, the primary barrier to nuclear entry is incompatibility between the channel size and capsid morphology. Analysis of the viral capsid structures docked at the NPC central channel further reveals the appearance of distinct striated patterns of lattice disorder along the surface of the capsid. This disorder, at the same time, represents a certain fragility of a more perfect lattice but also a form of capsid "flexibility" in terms of an entropic "spring-like" response to the stress imposed on the capsid by the NPC. To mimic the initiation of reverse transcription, we introduce a model for the viral genomic complex inside the capsids docked at the NPC. We find that in the uncondensed form, the genomic complex significantly amplifies the structural fragility of the pill-shaped capsid compared to the more canonical cone-shaped capsid.

Overall, our analysis of the intact viral capsids docked at the NPC demonstrates that the capsid lattice is pliable, but the structural integrity is also weakened during passage through the NPC central channel. The findings reported in this work elucidate several key factors that regulate the successful passage of viral capsid from the cytoplasmic to the nuclear end of the NPC.

## Results

**CG Model of Composite Membrane-Embedded Human NPC.** We developed CG models of the constricted and dilated states of human NPC from available experimental structural and biochemical data to surmount the computational costs associated with simulating a large macromolecular complex in atomic detail (22). The composite CG NPC models presented in this work consist of the outer CR and NR, and the IR (Fig. 1 *A* and *B*). The model development approach is largely bottom-up, i.e., constructed quantitatively from the underlying atomistic interactions generated from extensive all-atom (AA) MD simulation trajectories of NUP monomers and heterodimer subcomplexes. The statistics from the AA MD trajectories of NUP monomers were used to map CG molecular models with a mapping resolution of ~5 amino acids per CG site or "bead" (35). The same AA MD trajectories were used to derive a heterogeneous elastic network model of effective harmonic interactions to represent the intra-monomer interactions and maintain the protein molecular shape (36). Additionally, each CG bead had an excluded volume that allowed for maintaining the protein shape and preventing unphysical overlap between neighboring beads. Inter-monomer interactions within a subcomplex were phenomenologically modeled with a bonded soft elastic network model (harmonic force constant of 0.01 kcal $mol^{-1}$ $Å^{-2}$) derived directly from the cryo-ET structure. The choice of a weak force constant allows significant configurational flexibility while maintaining the overall shape of the subcomplexes. Inter-protein associative interactions at key binding interfaces between different NUP subcomplexes were modeled using nonbonded short-ranged attractive interactions derived from AA MD simulations of the corresponding heterodimer NUP complexes (37). Details of the AA MD simulations, model parameterization procedures, and CG model details are provided in the *Methods* and *SI Appendix*, Figs. S1–S3.

The CR and NR each consist of 8 copies of the dimerized Y-complex (Fig. 1*A*). The CG Y-complex consists of NUP133, NUP107, NUP96, SEC13, SEH1, NUP85, NUP43, NUP160, NUP37. Relative positions of the monomeric NUPs within a CG Y-complex and dimerization between the neighboring outer and inner CG Y-complex were maintained through a bonded soft elastic

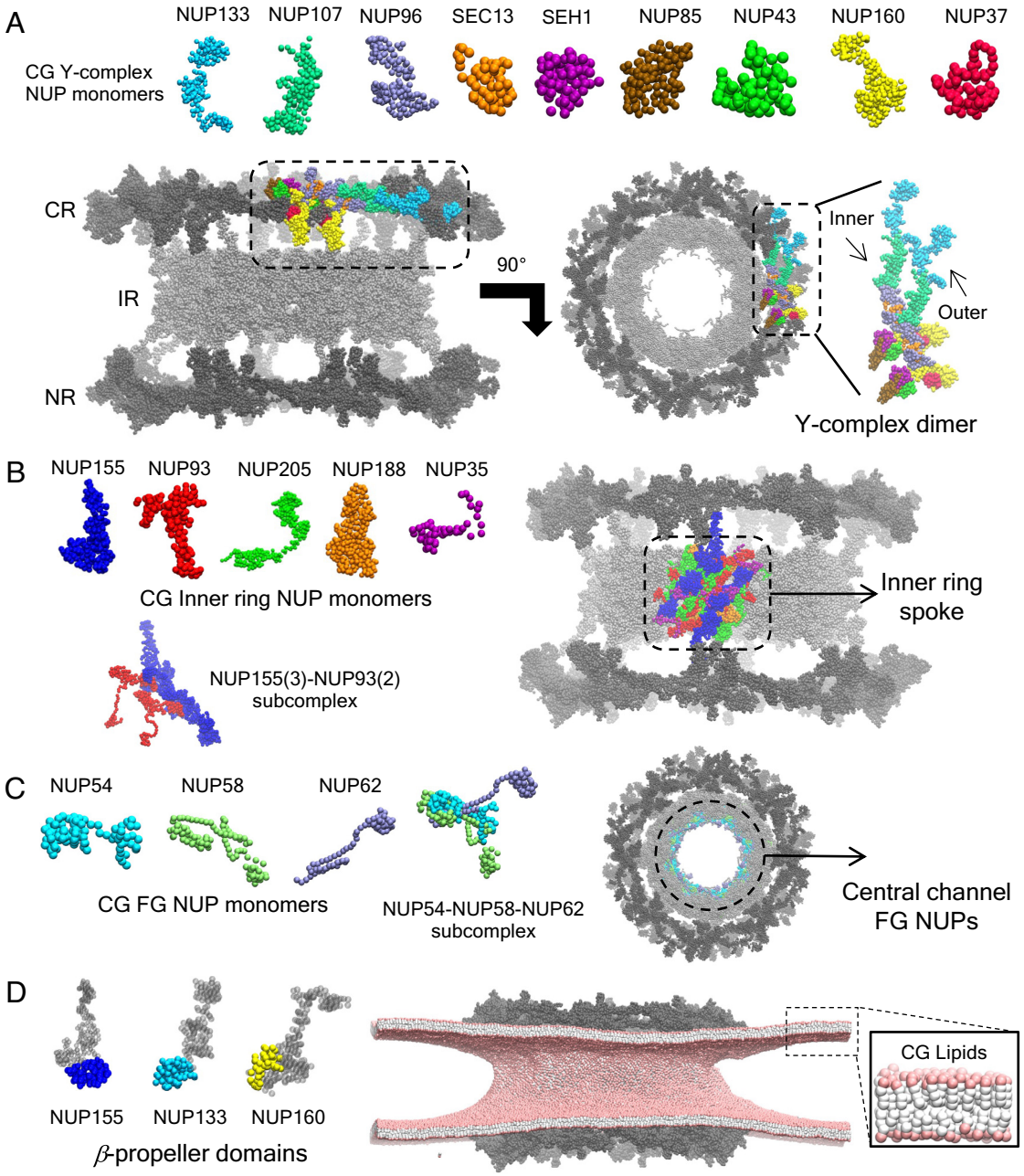


**Fig. 1.** Overview of the CG molecular model of the CR, NR, and IR. (*A*) The *Upper* panel shows the CG molecular model of each NUP monomer in the Y-complex. A side and top view of the NPC highlighting a single copy of the Y-complex dimer is shown in the *Lower* panel. The rest of the NPC is shown in gray spheres. The inner and outer Y-complex monomer is labeled in the Y-complex dimer. (*B*) CG molecular model of each NUP monomer in the IR is shown in the *Upper Left* panel. The NUP155–NUP93 subcomplex consisting of 3 copies of NUP155 and 2 copies of NUP93 is shown in the *Lower Left* panel. A single unit of the IR spoke is shown (*Right*) in the composite CG model of the NPC and is highlighted in color. (*C*) The CG molecular model of each FG NUP monomer and the NUP54–NUP58–NUP62 heterotrimeric subcomplex is depicted. A *Top* view of the NPC is shown, highlighting the FG NUPs NUP62 lining the central channel. (*D*) In the *Left* panel, the membrane binding $\beta$-propeller domains of NUP160, NUP133, and NUP155 are highlighted. The rest of the protein CG beads (no attractive interactions with lipids) are shown as gray spheres. In the *Right* panel, the membrane-embedded composite dilated NPC model is shown. In the *Inset*, the 4-site CG lipids are depicted. The headgroup of the CG lipid is shown in pink spheres. The interfacial CG bead and two tail beads of the CG lipid are shown in white spheres.

network model to allow configurational flexibility. Specifically, dimerization between an outer and inner Y-complex neighbor was maintained at the NUP133-CTD (inner)–NUP133-CTD (outer), SEC13 (inner)–NUP107-NTD (outer), and NUP160 (inner)–NUP96 (outer) interfaces. The head-to-tail oligomerization of the CG Y-complex dimers was modeled using non-bonded attractive interactions between a subset of CG sites at the NUP160–NUP133, NUP133–NUP37, and NUP107–NUP43 binding interface (*SI Appendix*, Fig. S1). The IR and CR/NR associations were modeled with attractive interactions between a subset of CG sites at the NUP155–NUP160 binding interface (*SI Appendix*, Fig. S2). In both cases, the subset of CG site pairs with attractive interactions at the binding interface was determined from the corresponding atomic residues involved in direct contacts in the AA trajectories.

The CG model of the IR complex consisted of NUP155, NUP93, NUP205, and NUP188 (Fig. 1*B*). The main building block of the CG IR spoke is a subcomplex composed of 3 adjacent copies of NUP155 and 2 copies of NUP93. Relative positions of monomers within this subcomplex were maintained with a bonded soft elastic network model. Interprotein interactions between NUP205 and

NUP188 monomers and the NU155–NUP93 subcomplex within a spoke and between spokes were modeled with non-bonded attractive interactions (*SI Appendix*, Fig. S3). Additionally, a polymer model of the NUP35 linker was used to connect the spokes. Phenylalanine-glycine (FG) containing channel nucleoporin NUP62 was modeled as a heterotrimeric subcomplex along with NUP54 and NUP58 (Fig. 1*C*). The NUP54–NUP58–NUP62 subcomplex (*SI Appendix*, Fig. S4) included a single copy of each protein, and each component within the subcomplex was connected through a bonded soft elastic network model. A total of 32 copies of NUP54–NUP58–NUP62 were anchored to the IR scaffold through non-bonded attractive interactions between NUP62 and NUP93 (NTD).

The nuclear membrane in our simulations was modeled by a 4-site CG lipid model (38). The parameters of the CG lipid are chosen such that the resulting bending rigidity of the membrane is 30 $k_BT$. We modeled the membrane association of the NPC through attractive interactions between the CG lipid head group and CG sites of the $\beta$-propeller domains of NUP160, NUP133, and NUP155 (Fig. 1*D* and *SI Appendix*, Fig. S5). In our CG model, the minimum protein–membrane interaction strength was chosen for which all the $\beta$-propeller domains remained associated with the membrane. We then simulated the composite membrane-embedded (*SI Appendix*, Figs. S4 and S5) constricted and dilated NPC model for 300 × $10^6$ CG MD timesteps ($\tau_{CG} = 50$ fs). From the final 150 × $10^6$ $\tau_{CG}$ timesteps, we estimated the CR, NR, and IR diameter. The mean diameters of the composite constricted and dilated CG NPC models closely reproduced the reference cryo-ET values (22), demonstrating the fidelity of our CG models (*SI Appendix*, Fig. S6).

**CG Simulations of HIV-1 Capsid Translocation into the NPC Central Channel.** We first derive the bottom-up CG capsid molecular model, CA-CA and CA-FG associative interactions (*SI Appendix*, Fig. S6). The FG-motif binding pocket is conserved across several host factors at the NPC (39). In this work, we consider that the FG sites in the N-terminal region (residue 1 to 150) of NUP62 also utilize the same binding pocket as the FG peptide from which the CA-FG interactions were derived. The initial atomic structure of the HIV-1 capsids was derived from cryo-ET images of capsids in intact virions and then mapped into CG structures (8, 40). To validate the CA-CA CG non-bonded associative interactions and whether these parameters maintain the capsid structural order, we simulated three different capsid morphologies (cone, pill, and ellipsoid). We characterized the capsid lattice order using neighbor-averaged Steinhardt's local bond order parameter ($\langle q_6 \rangle_{neigh}$) (41, 42) for each CA monomer (*SI Appendix*, Figs. S6 and S7). The $\langle q_6 \rangle_{neigh}$ values calculated from the CG MD simulations closely match that of the initial configuration mapped from the cryo-ET images (*SI Appendix*, Fig. S7), therefore, helping to further validate the accuracy of the CA-CA CG interactions used to model the HIV-1 capsid in this work.

Using the aforementioned CG models of HIV-1 capsid and membrane-embedded human NPC, we then performed CG MD simulations of capsid translocation into the NPC central channel (*Methods* and *SI Appendix*, Fig. S8). To perform the capsid translocation simulations into the NPC central channel, we implement a simulation protocol that is similar to parallel cascade MD (43). The simulation protocol used here allows for generating an effective trajectory (*SI Appendix*, Fig. S8) that represents the likely pathway of the capsid translocation instead of performing multiple replicate simulations, thereby reducing the overall computational expense. All capsid translocation simulations are performed with a cylindrical wall of 100 nm diameter (*SI Appendix*, Fig. S9) to restrict the diffusion of the capsid in the region coaxial to the central channel and reduce the available volume for capsid diffusion, thereby increasing the probability of translocation into the NPC central channel. The cylindrical wall emulates the confining effect of the cytoplasmic filaments, which are not included in the current model. A similar simulation setup was also used for the passage of small proteins into the NPC previously without the cytoplasmic filaments (44).

**Capsid Shape, the Orientation of the Approach, and Channel Dimension Determine Successful Translocation Events.** To examine the factors that regulate the translocation across the NPC central channel, we simulated the translocation dynamics of three capsid morphologies (cone, pill, and ellipsoid), all with both the dilated and the constricted state of the NPC. For the cone, we simulated two scenarios for which, in the initial configuration, either the narrow end or wide end was pointing to the central channel. Overall, we generated 8 distinct translocation trajectories from our simulations. The cumulative simulation time ranged between 400 to 1,200 × $10^6$ $\tau_{CG}$. We use two metrics to characterize the translocation –1. distance ($D_{Cap-NPC}$) between the geometric center of the capsid and equatorial midplane of the NPC IR along the channel axis, and 2. fraction of FG sites of NUP62 ($f_{FG-NUP62}$) directly in contact with the CA monomers. In Fig. 2 and *SI Appendix*, Figs. S10–S12, we show the time-series statistics of $D_{Cap-NPC}$ and $f_{FG-NUP62}$. A trajectory is classified as a successful docking event if, within 400 × $10^6$ $\tau_{CG}$, the tip of the capsid proximal to the NPC establishes long-lived contacts with the FG sites of NUP62 and $D_{Cap-NPC}$ progressively decrease with time. Conversely, in the unsuccessful trajectories, there are only transient contacts between the capsid and central channel within 400 × $10^6$ $\tau_{CG}$, and the capsid can backtrack toward the cytoplasmic side of the NPC, illustrating an unsuccessful docking attempt. In Fig. 3, we depict the final configuration of all eight distinct capsid translocation simulations performed in this study.

Our CG MD simulations reveal the behavior of different stages of translocation facilitated by the FG-NUPs of the central channel. The cone (approaching from the narrow end) and pill at the dilated NPC form significant contacts with the central channel FG-NUPs within 400 × $10^6$ $\tau_{CG}$. In contrast, both the cone (approaching from the narrow end) and pill only have nominal contacts with the central channel FG-NUPs within 400 × $10^6$ $\tau_{CG}$ at the constricted NPC. The cone (approaching from the wide end) and the ellipsoid capsid either only nominally associate or completely fail to associate with the central channel FG-NUPs for both the constricted and dilated state of the NPC. The early stages of the unsuccessful translocation dynamics trajectories reveal prolonged diffusion of the capsids at the cytoplasmic end of the NPC. However, the capsid tip in these unsuccessful translocation dynamics trajectories fails to translocate into the central channel.

We can rationalize the initial stages of capsid docking and translocation behavior by comparing the diameter of the central channel and the capsids examined in this study. The diameter of the IR scaffold, defined as the distance ($D_{NUP188}$) between the geometric center of the NUP188 at the IR of the opposite spokes, is 59 ± 7 nm and 73 ± 6 nm for the constricted and dilated states of the NPC, respectively. The capsid-binding FG-NUPs of the central channel are associated with the IR scaffold. Here, we approximate the void cross-section of the central channel as the distance between the geometric center of the NUP62 of the opposite spokes (Fig. 1*C*). The void cross-section of the central channel

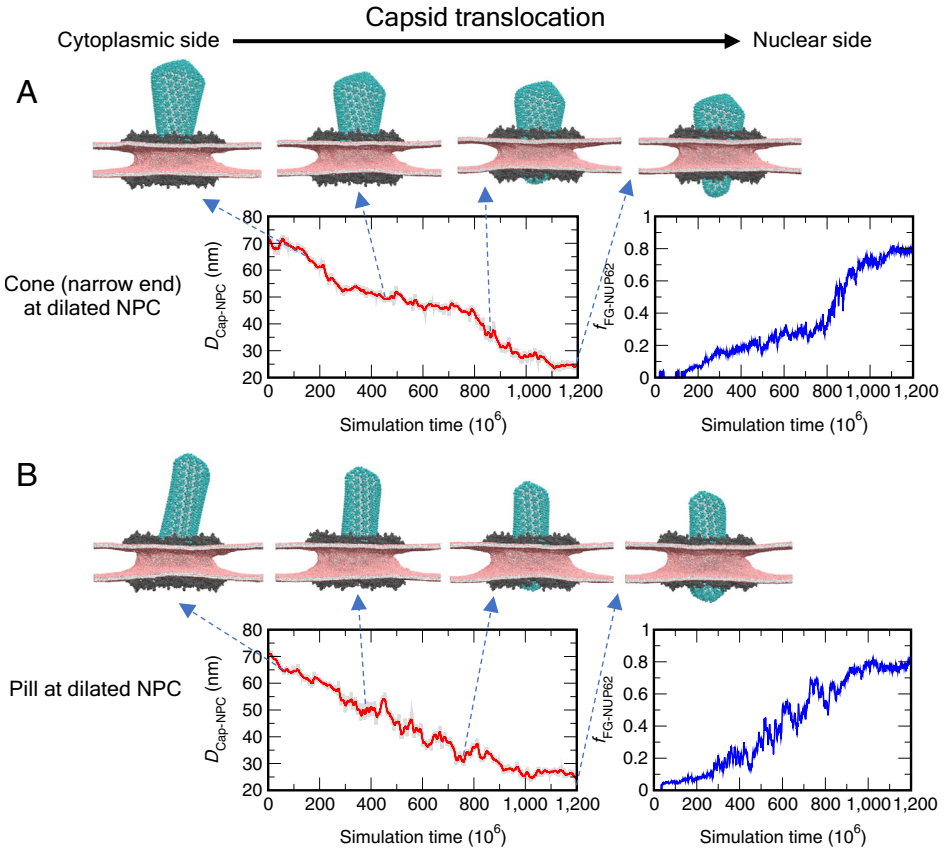


**Fig. 2.** Translocation dynamics of HIV-1 capsid into the NPC central channel. Translocation dynamics time series plot (*A* and *B*) that depicts the distance ($D_{Cap-NPC}$) between the geometric center of the capsid and NPC IR (*Left* panel in red), and the fraction of the FG sites of NUP62 ($f_{FG-NUP62}$) bound to CA (*Right* panel in blue). Note that each NUP62 consists of 15 FG-motif sites, and there are 32 NUP62 copies attached to the IR. The snapshots depict the translocation of the cone (approaching from the narrow end) and pill into the central channel of the dilated NPC from the cytoplasmic to the nuclear side at different points of the translocation trajectory. The NPC is shown in gray spheres. The NTD and CTD of the capsid is shown in cyan and white spheres. Lipids are shown in the color scheme as in Fig. 1.

available for the capsid to occupy is 41 ± 4 nm and 56 ± 6 nm for the constricted and dilated state of the NPC, respectively. The diameter of the cone at the narrow and wide end is 33 and 59 nm, respectively. The diameter of the pill and ellipsoid capsids are 42 and 56 nm, respectively. The diameter of the narrow end of the capsid cone is considerably smaller than the void cross-section of both the constricted and dilated states of the NPC; hence, the cone can spontaneously associate with the central channel of both constricted and dilated NPC in our simulations. The size compatibility also explains the association of the pill to the dilated state. After initial stable association to the central channel FG-NUPs is established, the cone and pill at the dilated NPC continuously translocate from the cytoplasmic to the nuclear end.

The time-series profiles of translocation from the cytoplasmic to the nuclear side of the NPC reveal key molecular insight into the factors that regulate successful passage (Fig. 2, Movies S1 and S2, and *SI Appendix*, Fig. S13). The cone initially undergoes a period of rapid passage through the central channel ($\tau < 300 \times 10^6\, \tau_{CG}$),

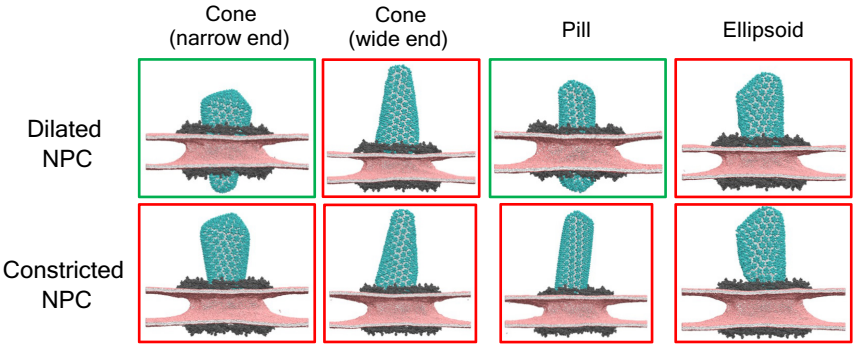


**Fig. 3.** Configurations from the endpoint of the translocation dynamics trajectory for all capsid shapes and orientations. A green-bordered panel shows the endpoint of a *successful* translocation trajectory in which the tip of the capsid translocates to the nuclear end. In our simulations, the cone (when approaching from the narrow end) and the pill at the central channel of the dilated NPC successfully translocate to the nuclear end. Endpoints of the rest of the trajectories are shown in red bordered panels. The capsid, NPC, and lipids are shown in the color scheme as in Fig. 2.

followed by a period during which the rate of translocation progressively slows down ($300 \times 10^6 < \tau < 800 \times 10^6\ \tau_{CG}$). In the final stages ($800 \times 10^6 < \tau < 1{,}100 \times 10^6\ \tau_{CG}$), the capsid again undergoes rapid passage. It is interesting to note that until $\tau < 800 \times 10^6\ \tau_{CG}$, the number of FG sites in contact with CA slowly and monotonically increases. After that, there is a sharp increase in the number of FG sites in contact with CA. We note that the maximum value of $f_{FG-NUP62}$ typically ranged from 0.8 to 0.85, which indicates that some NUP62 copies are sterically occluded by neighboring NUP54, NUP58, and other non-FG NUPs at the IR scaffold. We, therefore, propose that the translocation of the cone-shaped capsid adheres to the following successive steps: During the initial period of rapid translocation, the narrow end binds to the FG-NUPs of the central channel. The efficiency of passage gradually decreases as the central channel encounters the wider regions of the capsid. This can be attributed to the increasing steric interactions between the capsid and non-FG-NUPs of the central channel. In between $800 \times 10^6 < \tau < 1{,}100 \times 10^6\ \tau_{CG}$, the steep increase in the binding of FG sites to CA appears to facilitate rapid passage of the capsid cone. It also appears that at this stage, the adhesion between IR NUPs is loosened from the mechanical stress applied from the capsid allowing structural relaxation of the central channel. The consequent dilation of the channel assists in the accommodation of the wider regions of the cone. In contrast, the pill translocates into the central channel at a constant rate which can be attributed to its uniform cross-section. We estimate the NPC central channel diameter in the next section to elucidate the interplay between the structural relaxation of the channel and capsid translocation.

To summarize, our extensive CG MD results suggest that successful viral capsid passage across the NPC central channel is facilitated by the energetics of the capsid-binding FG-NUPs, while the primary barrier to translocation originates from the incompatibility between the channel dimension and capsid morphology.

**Progressive Dilation of the NPC Central Channel Facilitates Capsid Translocation.** To this point, we have established that the dilated state of the NPC allows passage of the cone-shaped and pill-shaped capsid. We next sought to characterize how mechanical stress arising from the translocation of the capsid impacts the IR scaffold structural organization. It is known that the IR spokes are capable of sliding movements under mechanical stress while preserving the arrangement of constituent NUPs within the spokes (45, 46). To analyze the structural change to NPC upon capsid translocation, we measure the diameter of the central channel. To perform the analyses, we divided the $1{,}200 \times 10^6\ \tau_{CG}$ long CG MD translocation trajectory of cone and pill-shaped capsid at the dilated NPC into 4 equal segments and labeled the segments Stage 1 to 4. The central channel diameter is defined as the distance between the geometric centers of NUP188 at the opposite spokes of IR (Fig. 4). Translocation of both cone (Fig. 4*A*) and the pill (Fig. 4*B*) causes additional dilation of the IR scaffold. However, the degree of dilation as a consequence of translocation for the cone-shaped capsid (~11%) is greater than the pill-shaped capsid (~7%) when the tips of the capsid reach the nuclear end (Stage 4). The higher degree of dilation of the channel for the translocation of the cone compared to the pill reflects the difference in size between the capsids (59 nm at the wide end of the cone and

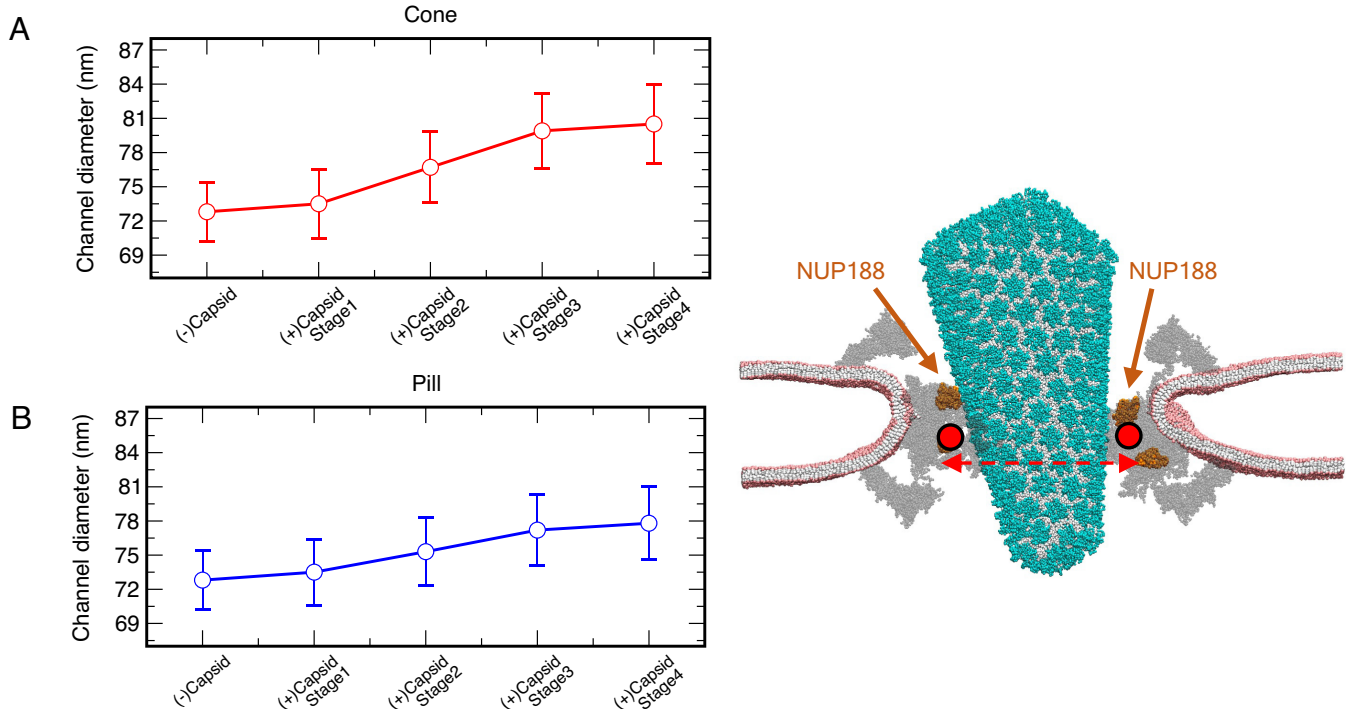


**Fig. 4.** NPC central channel diameter at different stages of capsid docking. Measurement of the central channel diameter for the translocation trajectories of the cone (*A*) and pill (*B*) into the dilated NPC. The channel diameter of the dilated NPC without capsid is calculated from the final $150 \times 10^6\ \tau_{CG}$ of a $300 \times 10^6\ \tau_{CG}$ CG MD trajectory. The data point (−)Capsid represents the channel diameter in the absence of the docked capsid. The translocation trajectory of cone (approaching from the narrow end) is divided into 4 equal sections to define four stages of capsid docking to the NPC central channel. The identical protocol is used to define the 4 stages of entry for the pill. The data points (+)Capsid Stage 1 to 4 represent capsid entry at different stages (same as also shown in Figs. 5 and 6). The data points report the mean and SD calculated over the $300 \times 10^6\ \tau_{CG}$ for each stage of the capsid translocation simulation. The *Right* panel shows the cutaway sideview of the NPC and lipid. The NUP188 of the IR is shown in orange spheres. The estimation of the channel diameter is performed between the geometric center of NUP188 of the opposite IR spokes (shown in the horizontal red dashed line). The mean channel diameter for the reference cryo-ET structure of the dilated NPC is 70.4 nm.

42 nm for the pill). Based on our analysis, it is evident that modest dilation of the IR scaffold is key to alleviating the steric stress and facilitating translocation of the capsid.

**Distinct Lattice Disorder Patterns Are Formed in Intact HIV-1 Capsids Docked at the NPC Central Channel.** Visual inspection of the capsid structures at the endpoint of the translocation trajectories revealed that the cone and the pill remained intact. To assess the stress impact of the spatially confined environment of the NPC central channel on the capsid structural state, we characterized the capsid lattice order using neighbor-averaged Steinhardt's local bond order parameter ($\langle q_6 \rangle_{neigh}$) (41) per CA monomer for the capsids docked at the dilated NPC. We considered the configurations at different stages of translocation (Fig. 2). To quantify the extent of disorder, we identified the CA monomers with $\langle q_6 \rangle_{neigh} < 0.4$ (*SI Appendix*, Fig. S7). We then estimated the size and organization of the disordered domains at different stages of translocation by performing clustering analysis and finally calculated the radius of gyration ($R_g$) of the largest disordered cluster. The four stages (1 to 4) are the same as defined in the previous section.

Isolated uncorrelated disordered domains are intrinsic to the capsid, observed both in the initial cryo-ET structure and in a free capsid in CG MD simulations (*SI Appendix*, Fig. S7). As the capsid approaches and associates with the central channel, we can identify distinct phases of weakening of the structural integrity of the capsid. Fig. 5 *B* and *C* display the average size of the largest contiguous disordered domain of CA monomers and the radius of gyration ($R_g$) at different stages of passage. Initially, the disordered domains grow independently of each other. The initial stages (1 and 2) encompass the approach of the capsid to the central channel at the cytoplasmic end to the first stable association to the FG-NUPs of the central channel. In the latter stages (3 and 4), the capsid translocates into the central channel driven by binding to the FG-NUPs while experiencing spatial confinement. In the latter stages, we observe a significant increase in the disordered domain size consisting of greater than 20 CA monomers (*SI Appendix*, Fig. S14). We attributed the growth of the disordered domains to the steric interactions of the capsid with the CR of the NPC scaffold. The disordered domains are large enough in size to anneal into well-defined striated patterns on the capsid lattice (Fig. 5 and *SI Appendix*, Fig. S15). The largest disordered domain contains

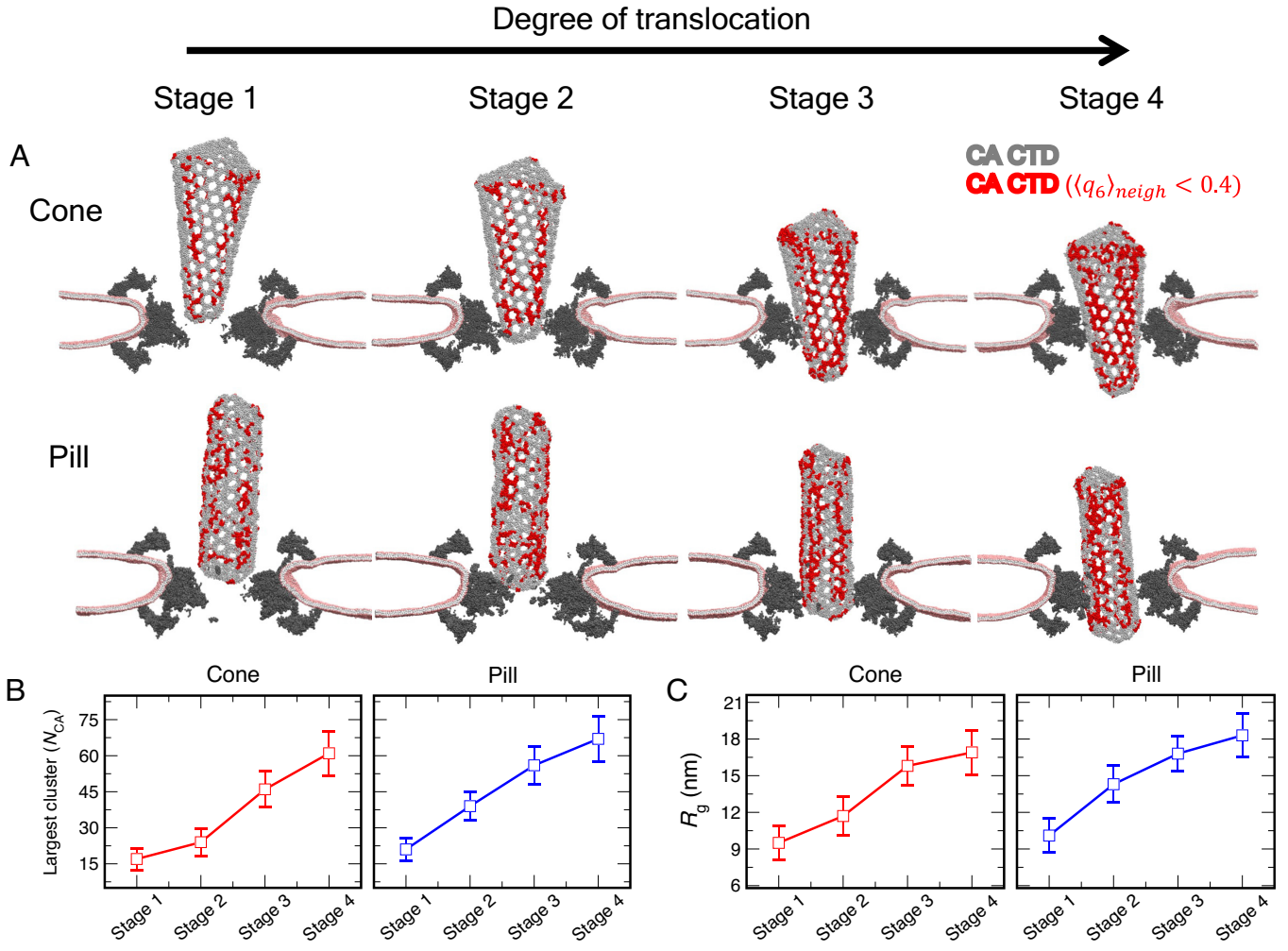


**Fig. 5.** Lattice disorder analysis of HIV-1 capsid at different stages of entry into the NPC central channel. (*A*) In each snapshot (at the endpoint of each stage), a cutaway sideview of the NPC (shown in gray spheres) and lipid bilayer is shown. The CTD of capsid is shown in silver spheres. The CTD of each CA monomer with $\langle q_6 \rangle_{neigh} < 0.4$ is shown in red spheres. Note, only the CTD is shown for clear depiction of the disordered patterns (in red). The snapshots correspond to the endpoint of the simulation at each stage (300, 600, 900, and 1,200 × $10^6$ $\tau_{CG}$). (*B*) Largest connected disordered cluster statistics of each stage for translocation of the cone and pill. Here, $N_{CA}$ is the number of CA monomers that constitute the largest connected disordered cluster in our analysis. (*C*) The radius of gyration ($R_g$) of the largest connected disordered cluster at each stage for translocation of the cone and pill into the central channel.

~60 CA monomers with a dimension up to ~20 nm when the tip of the capsid reaches the nuclear end. These striated disordered patterns on the capsid lattice are quite dynamic and undergo continuous rearrangement in the timescales of our CG MD simulation. Whether thermal fluctuations can lead to the stochastic nucleation of cracks at these striated disordered patterns will likely require significantly longer simulation timescales.

At this point, it is tempting to conclude that the lattice disorder of the capsid seen upon its translocation into the NPC is a measure of an "injured" capsid, that may in turn affect its later uncoating behavior within the nucleus. Such a conclusion indeed seems justified. We note that when docked at the central channel, in addition to the energetically favorable FG-NUP interactions, the capsid encounters non-FG-NUPs at a significantly higher frequency. The latter is energetically unfavorable and contributes to the stress of the capsid lattice. The ability of the capsid lattice to become more disordered upon experiencing the stress from its interaction with the NPC may also play a dual role. This disordering behavior is a sort of "structural elasticity" so that the capsid can better absorb the stress from the NPC interaction. Such behavior is often referred to as an "entropic spring" in which the increase in entropy (lattice disorder, i.e., $\Delta S < 0$) means the entropic component of the lattice free energy is lowered to a degree in response to the stress ($-T\Delta S < 0$). The structural elasticity can also be termed as the flexibility of the capsid shell. Without this flexibility, the lattice will behave as an assemblage of rigid objects. Therefore, the lattice would be very fragile in response to stress and can crack prematurely (in terms of the viral replication lifecycle), while within the NPC. We propose that future computational studies should aim to directly calculate the mechanical properties of the capsid under conditions of confinement to emulate the inward stress imparted by the NPC, which can then also be directly compared with experimental measurements (47).

## Condensation State of RNP Modulates the Lattice Disorder of HIV-1 Capsids

Recent studies have shown how the ribonucleoprotein (RNP) and eventual reverse transcription of the viral genome impact the structural integrity of the capsid (40, 48). Mature capsids encapsulate RNP complexes in a condensed globular form during viral assembly (49). Reverse transcription leads to uncoating and subsequent stiffening of the viral RNA. The increased spatial requirement of the genomic complex results in the loss of capsid patches allowing the extrusion of the newly synthesized DNA (18, 19, 48). To simulate capsids docked at the NPC (corresponding to Stage 4 in Fig. 5) with additional biological detail, we incorporated two polymeric chains in the capsid interior that minimally emulate two 9,000-nt RNP complexes. Modulating the interaction strength ($\varepsilon_{RNP}$) between the CG beads of the polymer allows for controlling the condensation state of the RNP. Additionally, CG beads of the RNP weakly interact with the C-terminal domain (CTD) tail of CA (*SI Appendix*, Fig. S9). We simulate the RNP in the capsid by varying $\varepsilon_{RNP}$ between 0.3 and 0.9 kcal/mol. For each $\varepsilon_{RNP}$ value, simulations are evolved for $80 \times 10^6\ \tau_{CG}$. We perform 3 replica simulations for each $\varepsilon_{RNP}$ for both the cone and pill. Here, our goal is to establish how different condensation states of the RNP impact the elastic response of the capsid docked at the NPC. The condensation states of the RNP in our simulations are intended to model the viral genome at different stages of uncoating prior to or at the initiation of reverse transcription.

Fig. 6 *A* and *B* summarize the results of the simulations of the RNP in the interior of the cone-shaped and pill-shaped capsid for different $\varepsilon_{RNP}$ values. Interestingly, the degree of RNP condensation, as characterized by the radius of gyration ($R_g$) of the polymer complex, appears to be sensitive to both $\varepsilon_{RNP}$ and the shape of the capsid (*SI Appendix*, Fig. S16). At $\varepsilon_{RNP}$ = 0.9 kcal/mol, the RNP spontaneously self-associates and forms a globular condensate (*SI Appendix*, Fig. S17). For the cone, the globular RNP localizes at the wide end in our simulations. Our simulations recapitulate the observation of imaging studies of preferential localization of the RNP at the wide end of the cone (49, 50), thus further establishing the validity of the minimal CG RNP model used in our studies. We find that for the pill, the RNP also condenses and localizes at the tip. For both the capsids, we attribute the preferred localization of the condensed RNP at the capsid tip to maximizing the contacts between the C-terminal end of CA and RNP beads at the surface of the condensate. Interestingly, in all the replica simulations, the condensed RNP in the pill localizes at the tip distal to the central channel. We speculate that the free and unconfined tip of the pill can undergo enhanced volume fluctuations which allows accommodation of the condensed RNP. At $\varepsilon_{RNP}$ = 0.6 kcal/mol, the RNP forms a partially condensed core with extended ends (*SI Appendix*, Fig. S17). At $\varepsilon_{RNP}$ = 0.3 kcal/mol, the RNP becomes fully uncondensed, associating with the C-terminal end of CA throughout the interior of the capsid (*SI Appendix*, Fig. S17). For the pill, at $\varepsilon_{RNP}$ = 0.9 kcal/mol, localization of the fully condensed RNP at the tip generates localized cracks (*SI Appendix*, Fig. S18). These cracks then lead to a degree of extrusion of the RNP in the uncondensed form ($\varepsilon_{RNP}$ = 0.3 kcal/mol). The appearance of these localized lattice cracks can be attributed to the significantly lower interior volume of the pill compared to the cone. We note that, despite the formation of localized cracks, the overall morphological integrity of the capsid is still preserved in our simulations, perhaps again reflecting a possible "entropic spring" behavior.

The condensation state of the RNP can create variable degree of internal mechanical stress on the capsid lattice in addition to external stress from the steric confinement arising from the central channel. To characterize the impact of the internal and external stress on the structural integrity of the capsid, we compute the lattice order of capsids docked at the NPC central channel at different RNP condensation states (Fig. 6*C*). The degree of RNP condensation has no significant effect on the largest disordered cluster for the cone. In contrast, there is a significant increase (~50%) in the largest disordered cluster size for the pill compared to when there is no RNP in the capsid interior. Our results demonstrate that the structural integrity of the pill is significantly weakened compared to the cone due to the lower interior volume of the former. We speculate that while both the cone and pill can successfully dock at the NPC central channel, the lattice packing of the pill is significantly weakened, which can lead to partial disassembly of the capsid during nuclear entry.

**Cohesiveness of Disordered NUP98 Impedes Capsid Association to the Central Channel.** The disordered FG-NUP98 is a component of the central channel that engages in multivalent cohesive interactions creating a hydrogel-like environment impacting the translocation dynamics of macromolecules (51–53). To investigate how the polymer-mesh characteristics of NUP98 chains regulate capsid association, we built a CG polymer model of $NUP98_{1\text{-}620}$ (*SI Appendix*, Fig. S3) and attached 48 NUP98 chains to the central channel. The updated model is called $NPC_{NUP98}$ (*SI Appendix*, Fig. S3). In our simulations, we modulated the NUP98 interaction strength ($\varepsilon_{NUP98}$) of the FG-rich regions between 0.2 and 1.0 kcal/mol and performed simulations for $60 \times 10^6\ \tau_{CG}$ for each $\varepsilon_{NUP98}$ (3 replicas).

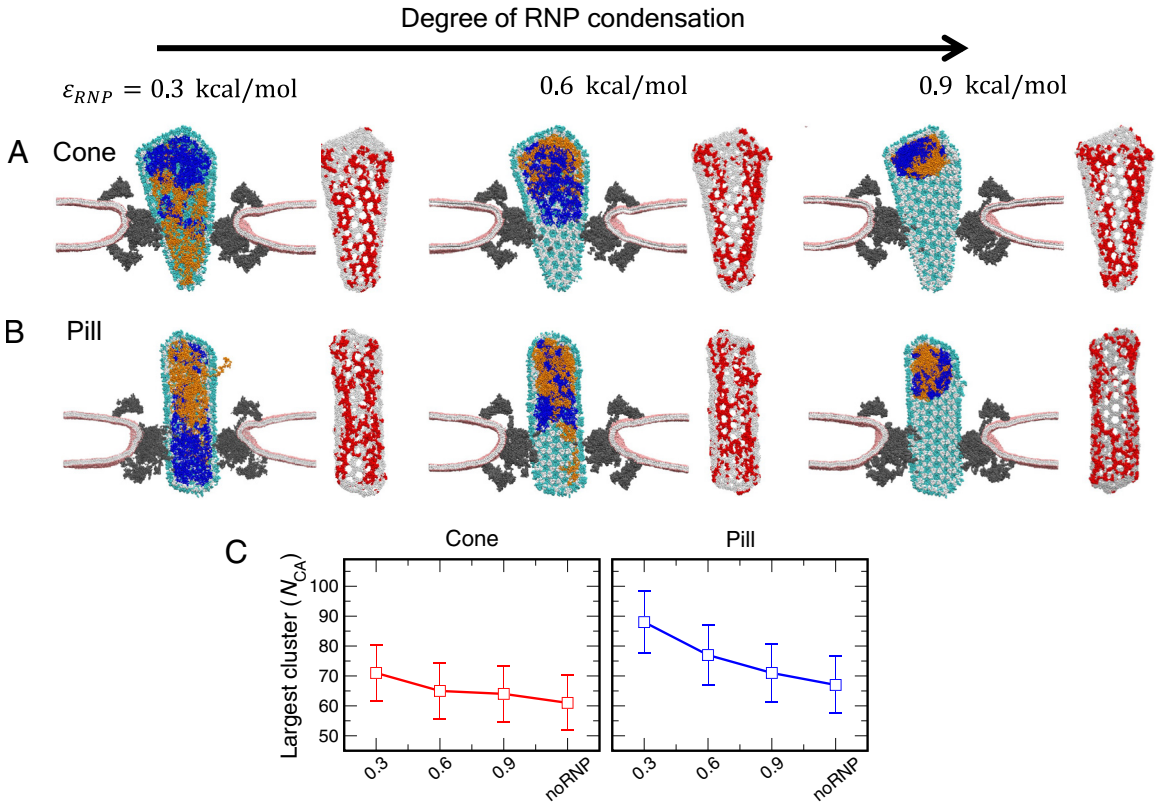


**Fig. 6.** Spatial localization of the RNP complex in the capsid interior docked at the central channel and lattice disorder analysis. In each snapshot, a cutaway sideview of the NPC and lipid is shown with the same colors as in Fig. 5. The capsid lattice is vertically sliced to show the RNP complex in the interior. The two RNP chains are shown in blue and orange spheres. From left to right, $\varepsilon_{RNP}$ is varied from 0.3 to 0.9 kcal/mol, thereby modulating the RNP condensation states. For both the cone (*A*) and pill (*B*), fully condensed RNP localizes at the capsid tip away from the NPC central channel. For each $\varepsilon_{RNP}$, the capsid with lattice disorder patterns is also shown on the side. The CTD of capsid is shown in silver spheres. The CTD of each CA monomer with $\langle q_6 \rangle_{neigh} < 0.4$ is shown in red spheres. The snapshots correspond to the endpoint of the simulation. (*C*) Largest connected disordered cluster statistics for each $\varepsilon_{RNP}$ value simulated in this study for the cone and pill.

*SI Appendix*, Fig. S19 summarizes the results of different cohesive states of NUP98 and the association of the narrow end of the conical capsid to the central channel. For the weaker $\varepsilon_{NUP98}$ interactions, the NUP98 chains formed extended configurations creating a highly dynamic and interactive mesh-like environment, most accurately mimicking the NUP98 conformations in the NPC environment in vivo (51). As the $\varepsilon_{NUP98}$ is increased, the NUP98 chains become gradually cohesive, forming local condensates. Importantly, the fraction of FG sites of NUP98 ($f_{FG-NUP98}$) in contact with the CA gradually diminishes with $\varepsilon_{NUP98}$. Our results present the following mechanistic picture. To successfully associate to the central channel, the capsid tip must permeate through the mesh-like medium of NUP98 chains and disrupt the inter-NUP98 interactions. Therefore, favorable CA-FG interactions must overcome the inter-NUP98 interactions that determine the cohesiveness of the mesh-like medium. As a result, capsid association with the NUP98 chains is only energetically feasible for weaker inter-NUP98 interaction strengths.

## Discussion and Concluding Remarks

How the NPC allows selective and efficient transport of large cargoes remains an important area of investigation. The mechanistic details of the nuclear import of the HIV-1 capsids, which have comparable dimensions to the NPC central channel, are yet to be fully understood. Importantly, the nuclear import step can be a key target for small molecule capsid inhibitors (20, 21). In this study, we computer simulations to elucidate the mechanisms that regulate the docking and translocation of the HIV-1 capsid into the central channel. Specifically, we explored how capsid morphology and orientation of approach regulate a successful translocation event. We observed successful translocation of conical and pill-shaped viral capsids for the dilated state of the NPC. Our simulations recapitulate recent visualization of intact capsids at the NPC central channel and nucleoplasm of infected and non-infected cells (18). Analysis of our translocation trajectories sheds light on the factors that are key to nuclear import and how the effective elasticity and structural integrity of the capsid are impacted. We anticipate that the mechanistic insights obtained in this work can also be broadly applied to infer the pathway of import of other large cargoes across the central channel of NPC.

The cross-section of the entire conical capsid is compatible with the dimension of the NPC central channel in the dilated state. One of our key findings is that despite the size compatibility of the entire cone and central channel in the dilated state, successful docking and translocation are contingent on the orientation of the capsid approach. Our simulations suggest that when approaching from the wide end and despite the size compatibility of the cone with the central channel, the initial steric barrier is too high to be surmounted by energetic contributions from interactions of CA with FG-NUPs (54). Furthermore, at the wide end of the cone, there are a higher number of available CA proteins for the channel FG-NUPs to bind relative to the narrow end, therefore providing a thermodynamic driving force for the association of the cone at the wide end. Hence, the inability of the cone in that orientation to translocate into the central channel is likely due to

a kinetic barrier. When approaching from the narrow end, the cone associates at the cytoplasmic end of the central channel and translocates till the tip of the capsid reaches the nuclear end. Importantly, the translocation of the cone continuously dilates the IR scaffold to progressively accommodate the wider regions of the cone. The preferred mechanism of the translocation of the capsid approaching from the narrow end is consistent with the in situ cryo-ET image of the HIV-1 core and capsid docking to NPC mimicking DNA-origami-based channel (18, 55). The binding of the capsid to the central channel generates outward stress. Therefore, progressive dilation of the central channel is key to increasing the effective void volume to accommodate a non-uniform shape cargo like the cone and reduce steric interactions. The IR scaffold architecture appears to be malleable enough to weaken the interactions between the constituent NUPs and allow dilation of the central channel under conditions of mechanical stress. Therefore, future experimental and enhanced sampling atomistic simulation studies are warranted to understand better how different NUP subcomplexes at the IR scaffold respond to mechanical stress and trigger large-scale conformational changes of the NPC (46).

Our implicit solvent CG MD simulations are designed to access timescales far beyond the capabilities of the fully atomistic simulations by reducing the number of particles. The dynamical timescales for capsid translocation from docking at the cytoplasmic end to the detection at the nuclear basket in GFP-labeled viral complexes are <1 h (17). Typically, the timescales in CG simulations are compared with experimental measurements by applying a scaling factor to match the corresponding frictional coefficients. A theoretical framework based on statistical mechanics to define the scaling factor for multicomponent biological systems is lacking (28). Therefore, we do not directly compare the timescales for capsid docking obtained from the CG simulations with experimental measurements.

We also analyzed how the capsid structural state is perturbed when translocating into the NPC central channel. Uncorrelated small, disordered domains are intrinsic to the capsid lattice. We find that when docked to the central channel, spatial confinement and steric interactions with central channel NUPs augment the number and the size of the disordered domains at the capsid lattice. Importantly, these isolated disordered domains anneal to highly correlated striated patterns on the capsid lattice. The presence of an uncondensed RNP in the capsid interior further amplifies the size of the correlated disordered domains on the lattice due to internal stress. The effect of the fully uncondensed RNP on lattice disorder is particularly significant in the case of the pill due to the lower interior volume when compared to the cone. Importantly, both cone and pill remain morphologically intact during translocation in the timescales of the CG MD simulations. Our results are consistent with the notion that primarily intact capsids enter through the central channel (18). Finally, our analysis indicates that while intact capsids dock at the central channel, the cone, in contrast to the pill, will most likely remain intact when captured at the nuclear basket.

As the capsid tip reaches the nuclear side of the NPC, it will encounter disordered NUP153 at the nuclear basket (56). NUP153 plays a key role in regulating the late stages of capsid nuclear entry (27, 57). Multiple recent studies have elucidated how NUP153 associates with HIV-1 capsid (58–60). It is noteworthy that NUP153 preferentially targets the high curvature regions of the capsid (60). Therefore, NUP153 chains tethered to the basket scaffold can bind to the capsid tip displacing the FG-NUPs of the central channel and pulling the entire capsid to the basket. A second key step of the nuclear import is the "handover" of the capsid from the nuclear basket to the interior of the nucleus (61). During the handover step, host factor CPSF6 localizes in high concentrations at the periphery of the basket, displaces NUP153, CPSF6 oligomerizes at the capsid resulting in the passage of the capsid to the nuclear interior (62, 63). Computational investigation of the mechanism of the translocation of the capsid from the central channel to the basket and the subsequent traversal to the nuclear interior will require the addition of the CG NUP153 and nuclear basket models to the NPC model developed in this work. A detailed high-resolution structure of the nuclear basket resolved by cryo-ET is yet to be reported and not included in our current model. Therefore, our current work focuses on the first step of the viral nuclear import dynamics, which is the docking of the capsid at the central channel. Direct visualization of viral nuclear import identified morphologically altered capsid shells that lack the internal genomic material, thereby indicating reverse transcription is the trigger for capture disassembly (18). In the future, it will be informative to investigate whether the capsid retains the lattice distortion patterns in the nuclear basket when there is no inward stress from the confining environment of the central channel. Furthermore, whether encountering NUP153 at high densities at the nuclear basket stabilizes or further perturbs the structurally fragile capsid after passage through the central channel will require future investigation, specifically the addition of the nuclear basket, as stated earlier.

The observation of the distinct disordered patterns on the capsid in our simulations docked at the NPC indicates a significant weakening of the structural integrity of the lattice (40), but at the same time, a certain overall capsid "plastic" response to the stress from the interaction of NPC components and uncondensation of the genomic material. It is known that nucleation of the first defect is the trigger for capsid rupture, while disassembly of capsomers progressively occurs post lattice rupture (64). The highly correlated striated patterns observed at the capsid lattice when docked at the central channel in our simulations can be the birthplace of defects leading to lattice disassembly during reverse transcription and release of viral genome (65). Experiments have identified antiviral small molecules PF74 and Lenacapavir, which associate with the capsid and mitigate reverse transcription (20, 64, 66). Both these compounds simultaneously contact adjoining CA monomers reducing fluctuations. Therefore, the likely mode of action of these small molecules is to stiffen the capsid lattice. We speculate that these molecules modulate the capsid intrinsic elasticity, rigidifying the lattice and resulting in premature lattice disintegration during nuclear import, as a rigidified capsid is unable to adapt to stress at the central channel.

Given the complexity of the human NPC, our current CG model consists of CR, NR, and IR. The human NPC also consists of the eight cytoplasmic filaments and capsid-binding FG-NUPs (NUP358, NUP214, and NUP88) localized at the cytoplasmic side (23, 67). The cytoplasmic filaments and the FG-NUPs at the cytoplasmic side likely play an important role in orienting the capsid for translocation into the central channel. The cytoplasmic filaments and the cytoplasmic FG-NUPs are not included explicitly in our current model. Thus, the initial configuration of the capsids in our simulations corresponds to the sequence of events after the FG-NUPs at the cytoplasmic side position the tip of the capsid to create optimal circumstances for interaction with central channel FG-NUPs. Our CG NPC model is also designed to represent the discrete constricted and dilated states. NPC is pleomorphic and explores multiple intermediate states between the constricted and dilated states under varying mechanical conditions triggered by conformational change of specific NUP subcomplexes (46, 68) and variation of nuclear membrane mechanical

properties (56, 57). One can also envision a scenario in which an intact capsid is docked at the dilated NPC, during which external perturbations constrict the central channel. In this case, the docked capsid will encounter additional inward stress, which may rupture the capsid. Multiple conformational states of constituent NPC subcomplexes can be modeled with a multiconfiguration coarse-graining framework, in which the degree of coupling between different CG conformational states reproduces the underlying all-atom free energy surface projected onto the CG coordinates (69). It will be valuable to incorporate these sophisticated features in our CG NPC model based on experimental structural data to investigate how dynamic variation of NPC conformation modulates dynamics of translocation and capsid structural integrity.

To summarize, in this work, we elucidated key factors that can regulate the successful translocation of the HIV-1 capsid into the NPC central channel. We find that capsid morphology and orientation of approach are key factors in regulating a successful translocation event. A successful translocation event is contingent on several sequential steps. First, the tip of the capsid, when approaching from the cytoplasmic end, must establish significant contact with the central channel FG-NUPs. Second, the capsid translocates if the morphology is compatible with the dimension of the channel driven by the energetics of the interaction between channel FG-NUPs and capsomers. Specifically, for the cone-shaped capsid, there is a gradient of the number of capsomers available to bind to the FG sites in the channel due to the non-uniform cross-section. However, the gradually increasing cross-section also presents an incremental steric barrier impeding translocation. We find that the progressive relaxation of the IR scaffold leading to the dilation of the channel serves to relieve the resulting steric barrier for translocation (46). Finally, we found that extended (not associated) configurations of disordered NUP98 as observed in vivo when tethered to the NPC, promote capsid association to the central channel. Our results indicate that energetically favorable interactions between FG-NUP98 and capsid reduce the initial association barrier of the capsid to the NPC central channel.

Structural analysis of the viral capsids associated with the NPC central channel also indicates the appearance of highly correlated striated patterns of lattice disorder. These disorder patterns are indicative of both a capsid structural pliability and the weakening of the capsid structural integrity as a consequence of the radial stress from the spatial confinement of the central channel and internal RNP. Our results demonstrate intrinsic lattice flexibility is an essential feature that allows the capsid to effectively absorb the stress and remain morphologically intact. Therefore, we predict that modulating the flexibility of the capsid may be an effective antiviral mechanism, rigidifying the capsid and reducing the likelihood of intact capsids translocating into the NPC and impairing infectivity. Once the capsid tip reaches the nuclear end of the NPC, the binding of the host factors NUP153 and CPSF6 mediate the nuclear import (27, 63). Furthermore, NUP153 and CPSF6, which are disordered proteins, form higher-order aggregates templated by the capsid (62, 70). How these host factors regulate the dynamics of capsid passage from the NPC central channel to the interior of the nucleus and modulate the capsid structural integrity will be the subject of future investigation.

## Methods

**CG Modeling and Simulation.** The details of the CG model development and details of the NPC, capsid, RNP, and lipid are described in *SI Appendix*. All CG MD simulations were prepared and simulated in the LAMMPS MD software (71). The details of the steps to construct the composite NPC-lipid system are described in *SI Appendix*, Fig. S5. All CG MD simulations were performed using a CG MD time step ($\tau_{CG}$) of 50 fs, and the equations of motions were integrated with the Velocity Verlet algorithm. All simulations were periodic in all three directions. Final production simulations were performed in the constant $Np_{xy}T$ ensemble. The temperature of the system was maintained using Langevin thermostat at 300 K with a coupling constant of 2,000 $\tau_{CG}$ (72). The pressure of the system was maintained using a Nose–Hoover barostat with a coupling constant of 4,000 $\tau_{CG}$ (73). Simulation trajectory snapshots were saved every $0.5 \times 10^6$ CG MD timesteps. Visualization of the simulation trajectories was performed in VMD (74). The details of capsid translocation simulations and the simulations of freely diffusing capsid are described in *SI Appendix*, Fig. S8.

**Data, Materials, and Software Availability.** The CG model parameters of the NPC and HIV-1 capsid, and input files are provided at https://doi.org/10.5281/zenodo.8217689 (75). All other data are included in the manuscript and/or supporting information.

**ACKNOWLEDGMENTS.** Computational resources were provided by the Texas Advanced Computing Center at The University of Texas at Austin and the Research Computing Center at The University of Chicago. Simulations were performed using resources provided by the Extreme Science and Engineering Discovery Environment (prior to September 2022), supported by the NSF grant number 1548562, by the Advanced Cyberinfrastructure Coordination Ecosystem: Services & Support program (after September 2022), which is supported by NSF grants numbers 2138259, 2138286, 2138307, 2137603, and 2138296, and Frontera (at TACC) funded by the NSF (OAC-1818253). This research was supported by National Institute of Allergy and Infectious Diseases of the NIH by grant U54 AI170855 for the Behavior of HIV in Viral Environments Center (A.H. and G.A.V.).

1. M. Lusic, R. F. Siliciano, Nuclear landscape of HIV-1 infection and integration. *Nat. Rev. Microbiol.* **15**, 69–82 (2017).
2. J. Rasaiyaah *et al.*, HIV-1 evades innate immune recognition through specific cofactor recruitment. *Nature* **503**, 402–405 (2013).
3. R. Welker, H. Hohenberg, U. Tessmer, C. Huckhagel, H.-G. Kräusslich, Biochemical and structural analysis of isolated mature cores of human immunodeficiency virus type 1. *J. Virol.* **74**, 1168–1177 (2000).
4. J. A. G. Briggs *et al.*, The stoichiometry of Gag protein in HIV-1. *Nat. Struct. Mol. Biol.* **11**, 672–675 (2004).
5. S. Li, C. P. Hill, W. I. Sundquist, J. T. Finch, Image reconstructions of helical assemblies of the HIV-1 CA protein. *Nature* **407**, 409–413 (2000).
6. B. K. Ganser, S. Li, V. Y. Klishko, J. T. Finch, W. I. Sundquist, Assembly and analysis of conical models for the HIV-1 core. *Science* **283**, 80–83 (1999).
7. M. Gupta, A. J. Pak, G. A. Voth, Critical mechanistic features of HIV-1 viral capsid assembly. *Sci. Adv.* **9**, eadd7434 (2023).
8. S. Mattei, B. Glass, W. J. H. Hagen, H.-G. Kräusslich, J. A. G. Briggs, The structure and flexibility of conical HIV-1 capsids determined within intact virions. *Science* **354**, 1434–1437 (2016).
9. J. A. G. Briggs, T. Wilk, R. Welker, H.-G. Kräusslich, S. D. Fuller, Structural organization of authentic, mature HIV-1 virions and cores. *EMBO J.* **22**, 1707–1715 (2003).
10. A. von Appen *et al.*, In situ structural analysis of the human nuclear pore complex. *Nature* **526**, 140–143 (2015).
11. Z. Ingram, M. Taylor, G. Okland, R. Martin, A. E. Hulme, Characterization of HIV-1 uncoating in human microglial cell lines. *Virol. J.* **17**, 31 (2020).
12. E. Hulme Amy, Z. Kelley, D. Foley, J. Hope Thomas, Complementary assays reveal a low level of CA associated with viral complexes in the nuclei of HIV-1–infected cells. *J. Virol.* **89**, 5350–5361 (2015).
13. I. Zurnic Bönisch *et al.*, Capsid-labelled HIV to investigate the role of capsid during nuclear import and integration. *J. Virol.* **94**, e01024–19 (2020).
14. A. C. Francis, G. B. Melikyan, Single HIV-1 imaging reveals progression of infection through CA-dependent steps of docking at the nuclear pore, uncoating, and nuclear transport. *Cell Host Microbe* **23**, 536–548.e6 (2018).
15. J. I. Mamede, G. C. Cianci, M. R. Anderson, T. J. Hope, Early cytoplasmic uncoating is associated with infectivity of HIV-1. *Proc. Natl. Acad. Sci. U.S.A.* **114**, E7169–E7178 (2017).
16. C. Li, R. C. Burdick, K. Nagashima, W.-S. Hu, V. K. Pathak, HIV-1 cores retain their integrity until minutes before uncoating in the nucleus. *Proc. Natl. Acad. Sci. U.S.A.* **118**, e2019467118 (2021).
17. R. C. Burdick *et al.*, HIV-1 uncoats in the nucleus near sites of integration. *Proc. Natl. Acad. Sci. U.S.A.* **117**, 5486–5493 (2020).
18. V. Zila *et al.*, Cone-shaped HIV-1 capsids are transported through intact nuclear pores. *Cell* **184**, 1032–1046.e18 (2021).
19. T. G. Müller *et al.*, HIV-1 uncoating by release of viral cDNA from capsid-like structures in the nucleus of infected cells. *Elife* **10**, e64776 (2021).
20. S. M. Bester *et al.*, Structural and mechanistic bases for a potent HIV-1 capsid inhibitor. *Science* **370**, 360–364 (2020).
21. J. O. Link *et al.*, Clinical targeting of HIV capsid protein with a long-acting small molecule. *Nature* **584**, 614–618 (2020).

22. S. Mosalaganti *et al.*, AI-based structure prediction empowers integrative structural analysis of human nuclear pores. *Science* **376**, eabm9506 (2022).
23. C. J. Bley *et al.*, Architecture of the cytoplasmic face of the nuclear pore. *Science* **376**, eabm9129 (2022).
24. S. Petrovic *et al.*, Architecture of the linker-scaffold in the nuclear pore. *Science* **376**, eabm9798 (2022).
25. A. Dharan, N. Bachmann, S. Talley, V. Zwikelmaier, E. M. Campbell, Nuclear pore blockade reveals that HIV-1 completes reverse transcription and uncoating in the nucleus. *Nat. Microbiol.* **5**, 1088–1095 (2020).
26. K. Bichel *et al.*, HIV-1 capsid undergoes coupled binding and isomerization by the nuclear pore protein NUP358. *Retrovirology* **10**, 81 (2013).
27. A. Matreyek Kenneth, A. Engelman, The requirement for nucleoporin NUP153 during human immunodeficiency virus type 1 infection is determined by the viral capsid. *J. Virol.* **85**, 7818–7827 (2011).
28. J. Jin, A. J. Pak, A. E. P. Durumeric, T. D. Loose, G. A. Voth, Bottom-up coarse-graining: Principles and perspectives. *J. Chem. Theo. Comp.* **18**, 5759–5791 (2022).
29. J. M. A. Grime *et al.*, Coarse-grained simulation reveals key features of HIV-1 capsid self-assembly. *Nat. Commun.* **7**, 11568 (2016).
30. A. J. Pak, J. M. A. Grime, A. Yu, G. A. Voth, Off-pathway assembly: A broad-spectrum mechanism of action for drugs that undermine controlled HIV-1 viral capsid formation. *J. Am. Chem. Soc.* **141**, 10214–10224 (2019).
31. A. Yu *et al.*, TRIM5α self-assembly and compartmentalization of the HIV-1 viral capsid. *Nat. Commun.* **11**, 1307 (2020).
32. A. J. Pak, M. Gupta, M. Yeager, G. A. Voth, Inositol hexakisphosphate (IP6) accelerates immature HIV-1 gag protein assembly toward kinetically trapped morphologies. *J. Am. Chem. Soc.* **144**, 10417–10428 (2022).
33. A. J. Pak *et al.*, Immature HIV-1 lattice assembly dynamics are regulated by scaffolding from nucleic acid and the plasma membrane. *Proc. Natl. Acad. Sci. U.S.A.* **114**, E10056–E10065 (2017).
34. A. J. Pak, A. Yu, Z. Ke, J. A. G. Briggs, G. A. Voth, Cooperative multivalent receptor binding promotes exposure of the SARS-CoV-2 fusion machinery core. *Nat. Commun.* **13**, 1002 (2022).
35. Z. Zhang *et al.*, A systematic methodology for defining coarse-grained sites in large biomolecules. *Biophys. J.* **95**, 5073–5083 (2008).
36. E. Lyman, J. Pfaendtner, G. A. Voth, Systematic multiscale parameterization of heterogeneous elastic network models of proteins. *Biophys. J.* **95**, 4183–4192 (2008).
37. M. S. Shell, The relative entropy is fundamental to multiscale and inverse thermodynamic problems. *J. Chem. Phys.* **129**, 144108 (2008).
38. J. M. A. Grime, J. J. Madsen, Efficient Simulation of Tunable Lipid Assemblies Across Scales and Resolutions. *arXiv [Preprint]* (2019). https://doi.org/10.48550/arXiv.1910.05362 (Accessed 11 October 2019).
39. S. V. Rebensburg *et al.*, Sec24C is an HIV-1 host dependency factor crucial for virus replication. *Nat. Microbiol.* **6**, 435–444 (2021).
40. A. Yu *et al.*, Strain and rupture of HIV-1 capsids during uncoating. *Proc. Natl. Acad. Sci. U.S.A.* **119**, e2117781119 (2022).
41. W. Lechner, C. Dellago, Accurate determination of crystal structures based on averaged local bond order parameters. *J. Chem. Phys.* **129**, 114707 (2008).
42. P. J. Steinhardt, D. R. Nelson, M. Ronchetti, Bond-orientational order in liquids and glasses. *Phys. Rev. B* **28**, 784–805 (1983).
43. R. Harada, A. Kitao, Parallel cascade selection molecular dynamics (PaCS-MD) to generate conformational transition pathway. *J. Chem. Phys.* **139**, 035103 (2013).
44. D. Winogradoff, H.-Y. Chou, C. Maffeo, A. Aksimentiev, Percolation transition prescribes protein size-specific barrier to passive transport through the nuclear pore complex. *Nat. Commun.* **13**, 5138 (2022).
45. T. Stuwe *et al.*, Architecture of the fungal nuclear pore inner ring complex. *Science* **350**, 56–64 (2015).
46. C. E. Zimmerli *et al.*, Nuclear pores dilate and constrict in cellulo. *Science* **374**, eabd9776 (2021).
47. M. G. Mateu, Mechanical properties of viruses analyzed by atomic force microscopy: A virological perspective. *Virus Res.* **168**, 1–22 (2012).
48. D. E. Christensen, B. K. Ganser-Pornillos, J. S. Johnson, O. Pornillos, W. I. Sundquist, Reconstitution and visualization of HIV-1 capsid-dependent replication and integration in vitro. *Science* **370**, eabc8420 (2020).
49. L. Woodward Cora, N. Cheng Sarah, J. Jensen Grant, Electron cryotomography studies of maturing HIV-1 particles reveal the assembly pathway of the viral core. *J. Virol.* **89**, 1267–1277 (2014).
50. J. Fontana *et al.*, Distribution and redistribution of HIV-1 nucleocapsid protein in immature, mature, and integrase-inhibited virions: A role for integrase in maturation. *J. Virol.* **89**, 9765–9780 (2015).
51. M. Yu *et al.*, Visualizing the disordered nuclear transport machinery in situ. *Nature* **617**, 162–169 (2023).
52. S. C. Ng *et al.*, Barrier properties of Nup98 FG phases ruled by FG motif identity and inter-FG spacer length. *Nat. Commun.* **14**, 747 (2023).
53. E. E. Najbauer, S. C. Ng, C. Griesinger, D. Görlich, L. B. Andreas, Atomic resolution dynamics of cohesive interactions in phase-separated Nup98 FG domains. *Nat. Commun.* **13**, 1494 (2022).
54. C. F. Dickson *et al.*, Karyopherin mimicry explains how the HIV capsid penetrates nuclear pores. *bioRxiv [Preprint]* (2023). https://doi.org/10.1101/2023.03.23.534032 (Accessed 24 March 2023).
55. Q. Shen *et al.*, Modeling HIV-1 nuclear entry with nucleoporin-gated DNA-origami channels. *Nat. Struct. Mol. Biol.* **30**, 425–435 (2023).
56. T. C. Walther *et al.*, The nucleoporin Nup153 is required for nuclear pore basket formation, nuclear pore complex anchoring and import of a subset of nuclear proteins. *EMBO J.* **20**, 5703–5714 (2001).
57. K. A. Matreyek, S. S. Yücel, X. Li, A. Engelman, Nucleoporin NUP153 phenylalanine-glycine motifs engage a common binding pocket within the HIV-1 capsid protein to mediate lentiviral infectivity. *PLoS Pathog.* **9**, e1003693 (2013).
58. Q. Shen *et al.*, The capsid lattice engages a bipartite NUP153 motif to mediate nuclear entry of HIV-1 cores. *Proc. Natl. Acad. Sci. U.S.A.* **120**, e2202815120 (2023).
59. R. T. Schirra *et al.*, A molecular switch modulates assembly and host factor binding of the HIV-1 capsid. *Nat. Struct. Mol. Biol.* **30**, 383–390 (2023).
60. J. C. V. Stacey *et al.*, Two structural switches in HIV-1 capsid regulate capsid curvature and host factor binding. *Proc. Natl. Acad. Sci. U.S.A.* **120**, e2220557120 (2023).
61. T. G. Müller, V. Zila, B. Müller, H.-G. Kräusslich, Nuclear capsid uncoating and reverse transcription of HIV-1. *Ann. Rev. Virol.* **9**, 261–284 (2022).
62. G. Wei *et al.*, Prion-like low complexity regions enable avid virus-host interactions during HIV-1 infection. *Nat. Commun.* **13**, 5879 (2022).
63. D. A. Bejarano *et al.*, HIV-1 nuclear import in macrophages is regulated by CPSF6-capsid interactions at the nuclear pore complex. *Elife* **8**, e41800 (2019).
64. C. L. Márquez *et al.*, Kinetics of HIV-1 capsid uncoating revealed by single-molecule analysis. *Elife* **7**, e34772 (2018).
65. S. Rankovic, J. Varadarajan, R. Ramalho, C. Aiken, I. Rousso, Reverse transcription mechanically initiates HIV-1 capsid disassembly. *J. Virol.* **91**, e00289-17 (2017).
66. K. M. R. Faysal *et al.*, Pharmacologic hyperstabilisation of the HIV-1 capsid lattice induces capsid failure. *bioRxiv [Preprint]* (2022). https://doi.org/10.1101/2022.09.21.508807 (Accessed 25 November 2023).
67. A. Dharan *et al.*, KIF5B and Nup358 cooperatively mediate the nuclear import of HIV-1 during infection. *PLoS Pathog.* **12**, e1005700 (2016).
68. A. P. Schuller *et al.*, The cellular environment shapes the nuclear pore complex architecture. *Nature* **598**, 667–671 (2021).
69. M. E. Sharp, F. X. Vázquez, J. W. Wagner, T. Dannenhoffer-Lafage, G. A. Voth, Multiconfigurational coarse-grained molecular dynamics. *J. Chem. Theory Comput.* **15**, 3306–3315 (2019).
70. S. Milles, E. A. Lemke, Single molecule study of the intrinsically disordered FG-repeat nucleoporin 153. *Biophys. J.* **101**, 1710–1719 (2011).
71. S. Plimpton, Fast parallel algorithms for short-range molecular dynamics. *J. Comput. Phys.* **117**, 1–19 (1995).
72. T. Schneider, E. Stoll, Molecular-dynamics study of a three-dimensional one-component model for distortive phase transitions. *Phys. Rev. B* **17**, 1302–1322 (1978).
73. G. J. Martyna, D. J. Tobias, M. L. Klein, Constant pressure molecular dynamics algorithms. *J. Chem. Phys.* **101**, 4177–4189 (1994).
74. W. Humphrey, A. Dalke, K. Schulten, VMD: Visual molecular dynamics. *J. Mol. Graph.* **14**, 33–38 (1996).
75. A. Hudait, Model and Code for: HIV-1 capsid shape, orientation, and entropic elasticity regulate translocation into the nuclear pore complex. [Data set]. Zenodo. https://doi.org/10.5281/zenodo.8217689. Deposited 5 August 2023.